

## Quantitative phase-field simulations of coarsening and growth in complex systems

N. Moelans\*, A. Serbruyns, J. Heulens, B. Blanpain, P. Wollants  
K.U.Leuven, Dept. of Metallurgy and Materials Engineering, Leuven, Belgium

L. Vanherpe, S. Vandewalle  
K.U.Leuven, Dept. of Computer Science, Leuven, Belgium

B. Rodiers  
LMS International, Leuven, Belgium

Keywords: microstructure, grain growth, Zener pinning, anisotropy, soldering

### Abstract

A quantitative phase-field model for the evolution of polycrystalline structures is presented. The model is able to treat concurrently grain growth, Ostwald ripening and growth driven by the relative stabilities of the bulk phases. The model allows the specification of energy and mobility for each interface individually. Simulation results are discussed for 3 industrially relevant applications, namely grain growth in the presence of second-phase particles, anisotropic grain growth in systems with a fiber texture and diffusion and coarsening of lead-free solder joints.

### Introduction

Many materials of industrial relevance are multi-component, consist of several phases with a different crystal structure and/or several grains with a different crystal orientation. Especially at elevated temperatures, where grain boundary movement and diffusion are considerable, the structures coarsen in time. Examples are grain growth and Ostwald ripening (driven by interfacial energy) and the growth of intermetallic precipitates in a supersaturated matrix or an intermetallic layer between 2 substrates (driven by bulk energy). As a result, the material properties change in time, which may or may not be desired.

The phase-field approach has proven to be powerful for simulating the morphological changes for different processes, such as solidification, precipitation, martensitic transformations and coarsening [1-3]. Characteristic for phase-field models is that interfaces are assumed to be diffuse and have a finite width. One advantage is that phase-field models can tackle the evolution of arbitrarily complex morphologies. While early applications were mostly qualitative and for simplified materials, currently, much more attention is given to quantitative aspects. To reduce the computational requirements, so called 'thin interface' phase-field models have been developed. In these models the interfacial width is considered as a numerical parameter that can be modified for numerical reasons without affecting other system properties, such as interfacial energy, diffusion behavior or bulk thermodynamic properties. In this way, it has become feasible to perform accurate 3D simulations for realistic dimensions.

A 'thin-interface' formulation for grain growth in single-phase systems was recently introduced by some of the authors [4]. This model can treat arbitrary misorientation and inclination dependence and allows us a high controllability of the accuracy of the simulation

results. In the present paper, this model for grain growth in single-phase materials is combined with a ‘thin-interface’ approach for multi-component alloys, which was originally developed by Tiaden et al. [5] and Kim et al. [6]. Furthermore, the implementation strategy and a number of applications are discussed. The reader is referred to [4] and [5-8] for a theoretical derivation of the approach.

## Model Formulation

### Model Variables

Assume a polycrystalline material with  $C$  components and different phases  $\alpha, \beta, \dots, \rho$  with different crystal orientations. It is furthermore assumed that pressure, temperature and molar volume are constant. The different grains are represented by a large set of non-conserved order parameter fields, which are a function of time  $t$  and spatial coordinates  $\mathbf{r}$ ,

$$\vec{\eta} = (\eta_{\alpha 1}(\mathbf{r}, t), \eta_{\alpha 2}, \dots, \eta_{\beta 1}, \eta_{\beta 2}, \dots, \eta_{\rho i}, \dots).$$

The first symbol in the subscript refers to the different phases (with a different crystal structure) and the second to different crystal orientations of the same phase. Furthermore,  $C-1$  independent conserved composition fields, representing the local mol fraction of one of the components, are used

$$\vec{x} = (x_1(\mathbf{r}, t), \dots, x_k, \dots, x_{C-1}).$$

### Thermodynamic Description

The total Gibbs energy  $F$  of a heterogeneous system is formulated as a functional of all field variables

$$\begin{aligned} F(\eta_{\alpha 1}, \dots, \eta_{\beta i}, \dots, \eta_{\rho i}, \dots, x_1, x_2, \dots, x_{C-1}) \\ = F_{int} + F_{bulk} \\ = \int_V \left[ mf_0(\eta_{\alpha 1}, \dots, \eta_{\beta i}, \dots, \eta_{\rho i}, \dots) + \frac{\kappa(\vec{\eta})}{2} \sum_{\rho i} (\nabla \eta_{\rho i})^2 \right] dV \\ + \int_V f_b(\eta_{\alpha 1}, \dots, \eta_{\beta i}, \dots, \eta_{\rho i}, \dots, x_1, x_2, \dots, x_{C-1}) dV \end{aligned} \quad (1)$$

where  $\sum_{\rho i}^*$  indicates a sum over all order parameter fields. The energy functional consists of a bulk contribution  $F_{bulk}$  and an interfacial contribution  $F_{int}$ . The functional  $f_0$  in the interfacial contribution is a fourth order polynomial of the order parameter fields

$$f_0(\vec{\eta}) = \sum_{\rho i} \left( \frac{\eta_{\rho i}^4}{4} - \frac{\eta_{\rho i}^2}{2} \right) + \frac{\gamma(\vec{\eta})}{2} \sum_{\rho i} \sum_{\sigma j \neq \rho i} \eta_{\rho i}^2 \eta_{\sigma j}^2 + \frac{1}{4}, \quad (2)$$

with degenerate minima, where  $f_0 = 0$ , at

$$\begin{aligned} (\eta_{\alpha 1}, \dots, \eta_{\alpha i}, \dots, \eta_{\beta i}, \dots) &= (1, \dots, 0, \dots, 0, \dots), \dots, \\ (0, \dots, 1, \dots, 0, \dots), \dots, (0, \dots, 0, \dots, 1, \dots), \dots \end{aligned} \quad (3)$$

corresponding to the different phases and different crystal orientations. The model parameters  $\kappa$ ,  $\gamma$  and  $m$  are related to the interfacial free energy  $\gamma_{\text{int}}$  (a physical property of the system) and the diffuse interface width  $\ell_{\text{int}}$  (chosen based on numerical considerations) as

$$\gamma_{\text{int}} = g(\gamma) \sqrt{m\kappa} \quad (4)$$

and

$$\ell_{\text{int}} = \sqrt{\frac{\kappa}{mf_{0,\text{int}}(\gamma)}}, \quad (5)$$

where  $g(\gamma)$  and  $f_{0,\text{int}}(\gamma)$  are evaluated numerically as described in [4]. To distinguish between different interfacial energies for different phase boundaries,  $\kappa$  and  $\gamma$  can be formulated as a function of the order parameter fields [4].

Following [5-8], the bulk free energy density  $f_b$  in the phase-field free energy description (1) is related to the molar Gibbs energies  $G_m^\rho(x_1, \dots, x_{C-1}, T^*)$  of the different phases as a function of composition and for temperature  $T^*$  as

$$f_b = \sum_{\rho} \left( \phi_{\rho} \frac{G_m^{\rho}(\vec{x}^{\rho}, T^*)}{V_m} \right) + \sum_{k=1}^{C-1} \tilde{\mu}_k \left( x_k - \sum_{\rho} \phi_{\rho} x_k^{\rho} \right), \quad (6)$$

with  $V_m$  the molar volume,  $\phi_{\rho}$  the local fraction of phase  $\rho$ ,  $\tilde{\mu}_k$  the inter-diffusion potential for component  $k$  and  $\vec{x}^{\rho} = (x_1^{\rho}, \dots, x_{C-1}^{\rho})$  virtual composition fields for the different phases. Different from the models in [5-8], the sum of the local values of the order parameter fields may be different from 1 at interfaces. Therefore, the local phase fractions  $\phi_{\rho}$  are calculated from the order parameter fields as

$$\phi_{\rho} = \frac{\sum_i \eta_{\rho i}^2}{\sum_i \eta_{\rho i}^2 + \sum_{\sigma \neq \rho} \sum_i \eta_{\sigma i}^2}. \quad (7)$$

The virtual composition fields  $x_k^{\rho}$  are calculated from the real composition fields  $x_k$ , so that

$$x_k = \sum_{\rho} \phi_{\rho} x_k^{\rho}, \quad k = 1 \dots C-1 \quad (8)$$

and

$$\tilde{\mu}_k = \frac{1}{V_m} \frac{\partial G_m^{\alpha}}{\partial x_k^{\alpha}} = \dots = \frac{1}{V_m} \frac{\partial G_m^{\rho}}{\partial x_k^{\rho}} = \dots, \quad k = 1 \dots C-1, \quad (9)$$

although the inter-diffusion potentials  $\square \mu_k$  may vary from point to point in space. It can be verified for relations (6)-(9) that within the bulk of a phase  $\rho$ ,  $x_k = x_k^\rho$  and  $G_m(x_k) = G_m^\rho(x_k^\rho)$ . Only at interfaces, the virtual composition fields differ from the real composition field. Thanks to restriction (9),  $f_b$  does not contribute to the interfacial energy. As a consequence, interfacial energy and thickness can be chosen independently by changing the parameters  $\kappa$ ,  $\gamma$  and  $m$ , and without affecting the bulk properties.

## Evolution Equations

The evolution of the non-conserved order parameter fields is assumed to follow

$$\frac{\partial \eta_{\rho i}}{\partial t} = -L(\bar{\eta}) \frac{\delta F(\bar{\eta}, \bar{x})}{\delta \eta_{\rho i}} = -L(\bar{\eta}) \left( m \frac{\partial f_0(\bar{\eta})}{\partial \eta_{\rho i}} - \kappa(\bar{\eta}) \nabla^2 \eta_{\rho i} + \frac{\partial f_b(\bar{\eta}, \bar{x})}{\partial \eta_{\rho i}} \right), \quad \forall \eta_{\rho i} \quad (10)$$

where  $L$  is a parameter related to the interface kinetics. For grain boundaries between grains of a same phase,  $L$  is related to the grain boundary mobility  $\mu_{int}$  and grain boundary velocity  $v_{int}$  as

$$\mu_{int} = \frac{L}{g(\gamma)} \sqrt{\frac{\kappa}{m}}, \quad (11)$$

and

$$v_{int} = \mu_{int} \gamma_{int} \left( \frac{1}{\rho_1} + \frac{1}{\rho_2} \right) = L \kappa \left( \frac{1}{\rho_1} + \frac{1}{\rho_2} \right), \quad (12)$$

with  $g(\gamma)$  a function of the model parameter  $\gamma$  [4]. For grain boundaries between grains of a different phase, the velocity depends on both the kinetics of the interfacial reactions (characterized by  $\mu_{int}$ ) and the diffusional transport of solutes. For the processes described in this paper, it can however be assumed that the movement of interfaces between different phases is diffusion controlled.  $L$  (or  $\mu_{int}$ ) is then taken large enough to obtain diffusion controlled interface movement, although not too large for numerical efficiency.

If cross interactions are ignored, the evolution of the composition fields  $x_k(\mathbf{r}, t)$  is given by diffusion equations of the form [5-8]

$$\frac{1}{V_m} \frac{\partial x_k}{\partial t} = \nabla \cdot \sum_{\alpha} M_k(\bar{\eta}) \nabla \frac{\partial f_b}{\partial x_k} = \nabla \cdot \sum_{\rho} \phi_{\rho} M_k^{\rho} \nabla \square \mu_k, \quad k = 1 \dots C-1, \quad (13)$$

with

$$M_k^{\rho} = \frac{D_k^{\rho}}{\frac{\partial^2 G_m^{\rho}}{\partial x_k^2}}, \quad (14)$$

equations (14) reduce to the phenomenological diffusion equation of Fick.

## Parameter Determination and Numerical Implementation

### Parameter Determination

For all interfaces, the parameters  $\gamma$ ,  $\kappa$ ,  $m$  and  $L$  are calculated iteratively for given interface energies  $\gamma_{int}$ , mobilities  $\mu_{int}$  and a constant diffuse interface thickness  $\ell_{gb}$ . The iterative procedure is described in [4] and implemented in Matlab.

If parabolic functions of the form

$$\frac{G_m^\rho}{V_m} = \sum_{k=1}^{C-1} \frac{A_k^\rho}{2} (x_k - x_{k,0}^\rho)^2 + C^\rho \quad (15)$$

with  $A_k^\rho$ ,  $C_k^\rho$  and  $x_{k,0}^\rho$  model parameters, are used for the Gibbs energies of the different phases, equations (8) and (9) result in a linear system of equations with the virtual composition fields as unknowns, which can be solved efficiently. The parameters in the parabolic Gibbs energy expressions (15) are obtained by fitting expressions (17) to Gibbs energy expressions from thermodynamic databases (obtained according to the CALPHAD method [9]) within the composition range of interest, namely around the equilibrium compositions of the coexisting phases. For  $x_k < 10^{-12}$  or  $x_k > 1-10^{-12}$ , the  $A_k^\rho$  are taken 10 times larger than in the parabolic description fitted for phase  $\rho$ , to prevent the molar fraction of a component from taking an unphysical value beyond 0 or 1. With Gibbs energy expressions (15), constant parameter values for  $M_k^\rho$  result in constant diffusion coefficients  $D_k^\rho$  for the different bulk phases.

### Implementation Methodology

With respect to implementation, the approach is to combine an easily extensible and high-level program with the possibility to optimize it for specific applications. Therefore a C++ implementation has been implemented, which is a combination of an object-oriented and template metaprogramming [10-11] design. Different simulation methods considering different aspects of the model or using different numerical approaches, form different classes (called *simulation classes*), all with a common interface. There is one *simulation class* that considers the full model and is based on a central second-order finite difference discretization in space with first order explicit time stepping. Furthermore, there are specialized *simulation classes*; for instance, one using a semi-implicit Fourier-spectral method [12], which is most efficient for grain growth in isotropic systems (with or without fixed particles), and a ‘bounding box’ implementation for 3D grain growth simulations with many grains (see below). Other components, such as 2D and 3D data structures and a general interface for communication between different nodes, have been developed for use in the *simulation classes*. The 2D and 3D data-structures (matrices and tensors) were developed based on the principles of template metaprogramming and expression templates [13]. In this way abstraction is made of the implementation details of basic matrix and tensor algorithms, while keeping the same performance as hand-tuned for-loops that take caching mechanisms of processor caches into account. Similarly the communication between the nodes of a cluster is implemented in a class

hierarchy that allows modifying the parallelization mechanisms without having to rewrite the *simulation classes*. In practice, the MPI protocol is most often used.

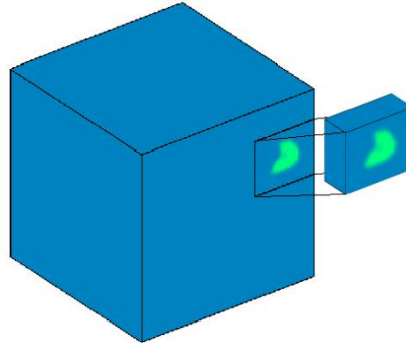


Figure 1: Illustration of the bounding box algorithm. The evolution equation of each phase field variable is solved only for a small box around the grain represented by the phase field variable.

The bounding box data structure has been designed specifically for polycrystalline structures [14]. It exploits the fact that at each point in the system only a limited number of order parameter fields differ from zero. It allows the use of a large number of order parameter fields (for representing all grains) without excessive memory usage or computational requirements. An order parameter field is defined to be *active* at a particular grid point when its value is larger than a small threshold value  $\varepsilon$ . Hence, within a grain only 1 order parameter field and near grain boundaries, only a few, namely those corresponding to the neighboring grains, are active. For each grain, a bounding box  $B_i$  is established as the smallest cuboid containing all grid points for which  $\eta_i > \varepsilon$  (see Figure 1). Within each time step, the evolution equation for  $\eta_i$  is solved numerically only for the grid points in box  $B_i$ , using a second-order central finite difference discretization in space and a first order semi-implicit time stepping. Then, the algorithm checks whether the grain regions have shrunk or grown, and updates the bounding boxes accordingly. The values of the order parameter fields are only stored for the grid points where they are active. The implementation is based on an object-oriented data structure as shown in the Unified Modelling Language (UML) diagram in Figure 2. The approach can easily be extended to more complex phase field models and has definite advantages in post-processing.

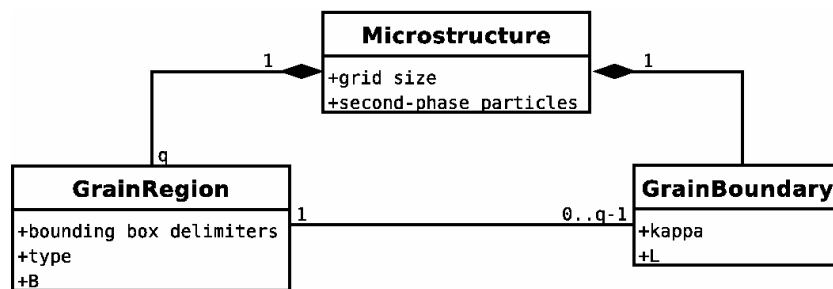


Figure 2: UML diagram of the object-oriented bounding box structure. The microstructure, grain regions and grain boundaries are treated as objects with a number of attributes, reflecting system properties, simulation parameters and bounding box delimiters.

## Applications

### Zener Pinning

The pinning effect of second-phase particles is a vastly employed mechanism to control the grain size of a material, which is for example used in the manufacturing of high-strength low-alloyed steels, where a small grain size is required to obtain high strength, toughness and deformability. The particles exert a pinning force on moving grain boundaries and therefore reduce their mobility and, when a final grain size  $R_{lim}$  is reached, arrest grain growth.

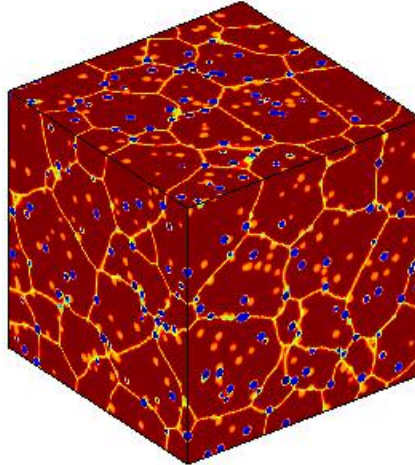


Figure 3: Snapshot of a 3D simulation of grain growth in a system with second-phase particles for a particle fraction  $f_v = 0.08$  and radius  $r = 4.3$  g.p. System size is  $256 \times 256 \times 256$  g.p.

2D [15] and 3D [14,16] simulations of grain growth in the presence of second-phase particles have been performed for different volume fractions  $f_v$  and radii  $r$  of the particles. The particles were assumed to be constant in time. The evolution of the average grain size, grain size distribution and the number of particles located on a grain boundary can be determined from the simulations, as well as the final grain size  $R_{lim}$  where grain growth stagnates. The simulation image in Figure 3 was obtained using the bounding box algorithm. Thanks to an efficient memory use, it is possible to perform simulations for systems with  $256 \times 256 \times 256$  grid points (g.p) and an arbitrary number of grains on a single node. Figure 4 shows, for different volume fractions, how the average grain size changes in time and finally stagnates.

### Grain growth in systems with a fiber texture

Thin films and wires have often a grain structure in which all crystals have nearly identical orientation in one direction, but are randomly oriented in the plane perpendicular to it. This structure is usually induced by geometrical symmetries in the deposition technique or deformation process. Due to the axi-symmetry, the orientation of the grains and misorientation between different grains can be expressed with a single angle.

Simulation results are shown for a system with misorientation dependence of the grain boundary energy as plotted in the upper graph in Figure 5. It assumes a four-fold symmetry. The orientations within one quadrant are

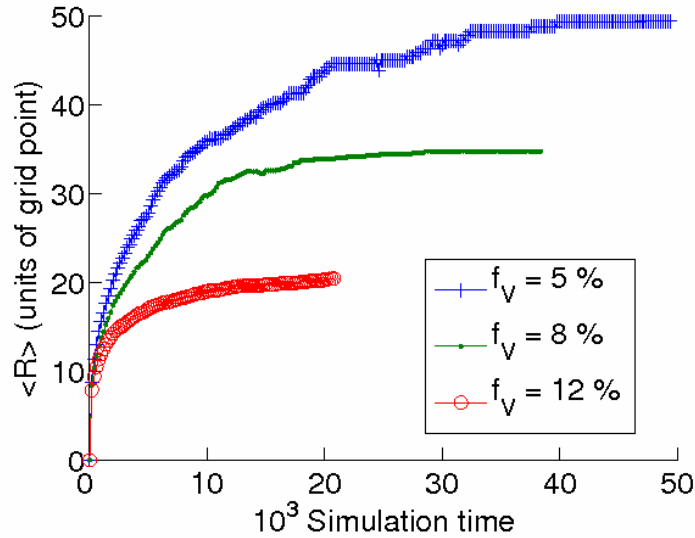


Figure 4: Temporal evolution of the mean grain size, as obtained from phase field simulations of grain growth in the presence of second-phase particles. When a limiting grain size  $R_{lim}$  is reached, grain growth stops.

discretized with an interspacing of  $1.5^\circ$  and assigned to 60 order parameters. The misorientation between grains with orientations  $i$  and  $j$  is calculated as  $\theta = 1.5^\circ |j-i|$  for  $|j-i| \leq 30$  and  $\theta = -90^\circ + 1.5^\circ |j-i|$  for  $|j-i| \geq 30$ . The grain boundary mobility is taken constant,  $\mu_{gb} = 1 \cdot 10^{-6} \text{ m}^2/\text{s}/\text{kg}$ , and the grain boundary width is taken  $\ell_{gb} = 1.33 \cdot 10^{-6} \text{ m}$ . Calculation of the model parameters using the iterative algorithm from [4] with  $\gamma_{init} = 1.5$  and  $\sigma_{gb,init} = 0.25 \text{ J}/\text{m}^2$ , gives  $m = 2.25 \cdot 10^6 \text{ J}/\text{m}^3$ ,  $L = 1 \text{ ms}/\text{kg}$  and values for  $\kappa$  and  $\gamma$  as a function of misorientation as shown in Figure 5. The simulations can be performed with the general *simulation class* or with the bounding box algorithm. A grid spacing  $\Delta x = 0.2 \cdot 10^{-6} \text{ m}$  and time step  $\Delta t = 0.008 \text{ s}$  were used. Figure 6 shows the grain structure at  $t = 144 \text{ s}$ . In Figure 7, it is shown how the grain boundary character distribution changes in time. The simulations start from a random grain boundary character distribution. The fraction of low-angle boundaries increases in time. The fraction of boundaries with a misorientation close to  $37.5^\circ$  increases in the beginning, but then starts decreasing again. It may be expected that finally a steady-state growth regime with constant grain boundary character distribution is reached.

### Diffusion and Coarsening in Cu/Sn-0.02at% Cu Solder Joints

During soldering, typically an intermetallic compound (IMC) is formed between the molten solder and the solid substrate. Due to diffusion the IMC and intermetallic precipitates in the solder alloy continue to grow during device use. Because of their inherent brittle nature, the morphology and thickness/size of the IMC layer and precipitates strongly affect the mechanical properties of the solder joint.

Simulations were performed for a Cu-substrate / Sn-0.02at%Cu-solder joint. For all phases, the interfacial energy is taken  $\gamma_{int} = 0.35 \text{ J}/\text{m}^2$ , the interface mobility  $\mu = 3 \cdot 10^2 \text{ m}^2/\text{s}/\text{kg}$  and interfacial width  $\ell_{gb} = 5 \cdot 10^{-7} \text{ m}$ . A (Cu)-phase, a (Sn)-phase and an intermetallic  $\text{Cu}_6\text{Sn}_5$ -phase

are considered, the  $\text{Cu}_3\text{Sn}$ -phase is not. Based on phase diagram information and Gibbs energy expressions (SSOL4 database [17]) for  $T^*=150^\circ\text{C}$ , the following parameters in the parabolic free energies were chosen:  $A^{(\text{Cu})}=10^8$ ,  $C^{(\text{Cu})}=0$ ,  $x_{0,\text{Sn}}^{(\text{Cu})}=0.076$ ,  $A^{(\text{Sn})}=10^9$ ,  $C^{(\text{Sn})}=10^7$ ,  $x_{0,\text{Sn}}^{(\text{Sn})}=0.979$ ,  $A^{\text{Cu}_6\text{Sn}_5}=10^{10}$ ,  $C^{\text{Cu}_6\text{Sn}_5}=-10^6$ ,  $x_{0,\text{Sn}}^{\text{Cu}_6\text{Sn}_5}=0.455$ . The parabola are plotted in Figure 8. The inter-diffusion coefficients are taken as  $D_{\text{Sn}}^{\text{Cu}_6\text{Sn}_5}=0.5\cdot 10^{-16}\text{ m}^2/\text{s}$  and  $D_{\text{Sn}}^{(\text{Cu})}=D_{\text{Sn}}^{(\text{Cu})}=0.5\cdot 10^{-12}\text{ m}^2/\text{s}$ .

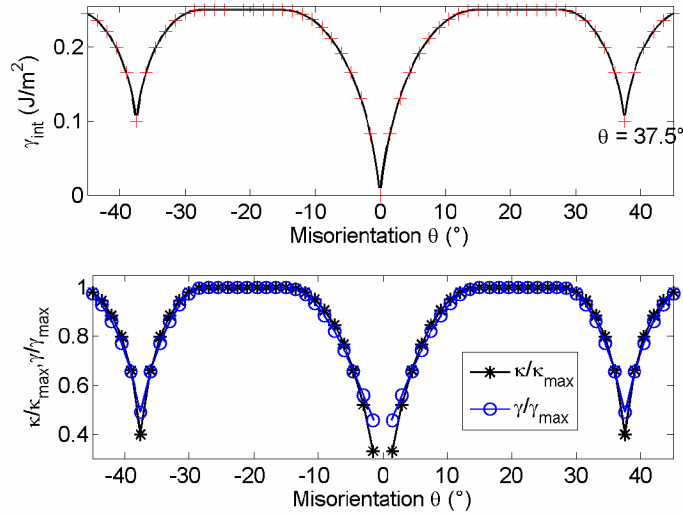
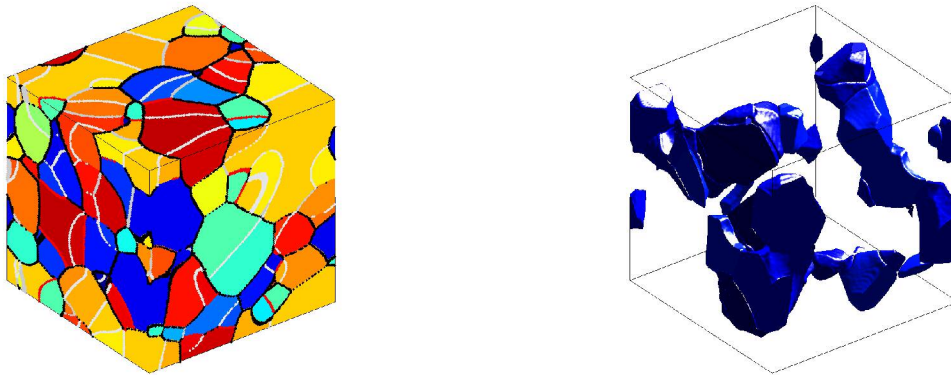


Figure 5: Upper: Grain boundary energy as a function of misorientation used in the simulations for structures with fiber symmetry. For low-angle misorientations a Read-Shockley dependence with  $\theta_m=15^\circ$  and  $\sigma_m = 0.25\text{ J/m}^2$  is assumed. Furthermore, there is a low-energy cusp at  $37.5^\circ$ . Lower: Model parameters  $\kappa$  and  $\gamma$  as a function of misorientation.



a)

b)

Figure 6: a) Snapshot of a 3D grain growth simulation. Grains with similar orientation have a similar color. Boundaries with misorientation  $1.5^\circ$ ,  $3^\circ$  and  $37.5^\circ$  are respectively indicated in white, gray and red. System size is  $200\times 200\times 200\text{ g.p.}$  which represents  $64000\text{ }\mu\text{m}^3$ . b) 3D view of clusters of grains with a similar orientation. The blue grains correspond to the blue grains in a).

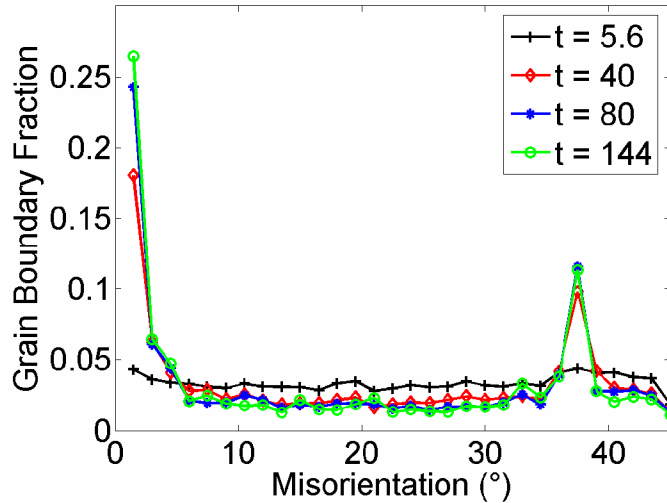


Figure 7: Temporal evolution of the grain boundary character distribution.

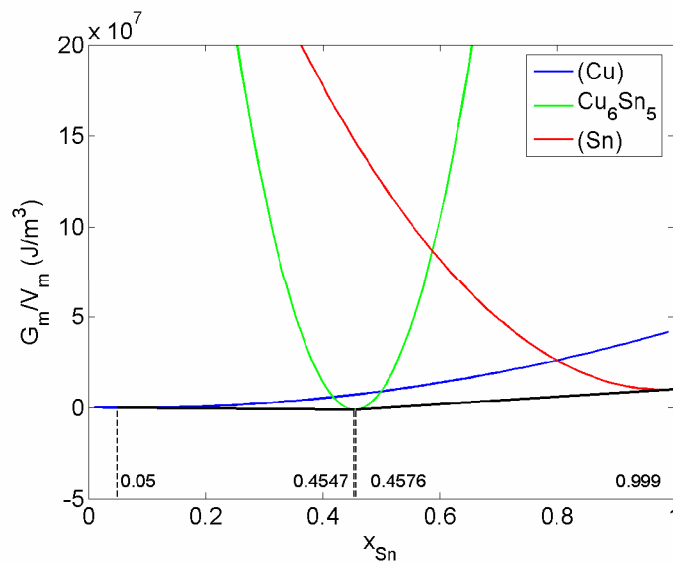


Figure 8: Parabolic free energies for the (Cu), (Sn) and  $\text{Cu}_6\text{Sn}_5$ -phase used in the simulations of the lead-free solder joint. The equilibrium compositions of the coexisting phases, determined by the common tangent construction, are also indicated.

The simulation images in Figure 9 show how the intermetallic  $\text{Cu}_6\text{Sn}_5$ -layer grows, consuming the (Cu) and (Sn) phases, by diffusion through the intermetallic layer. At the same time the intermetallic  $\text{Cu}_6\text{Sn}_5$ -precipitates undergo Ostwald ripening by Cu diffusion through the Sn-matrix. The volume fraction of the precipitates is initially 0.04 (according to the lever rule), but decreases in time as part of the Cu-atoms dissolved in the Sn-matrix re-precipitate on the intermetallic layer (and not on a precipitate).

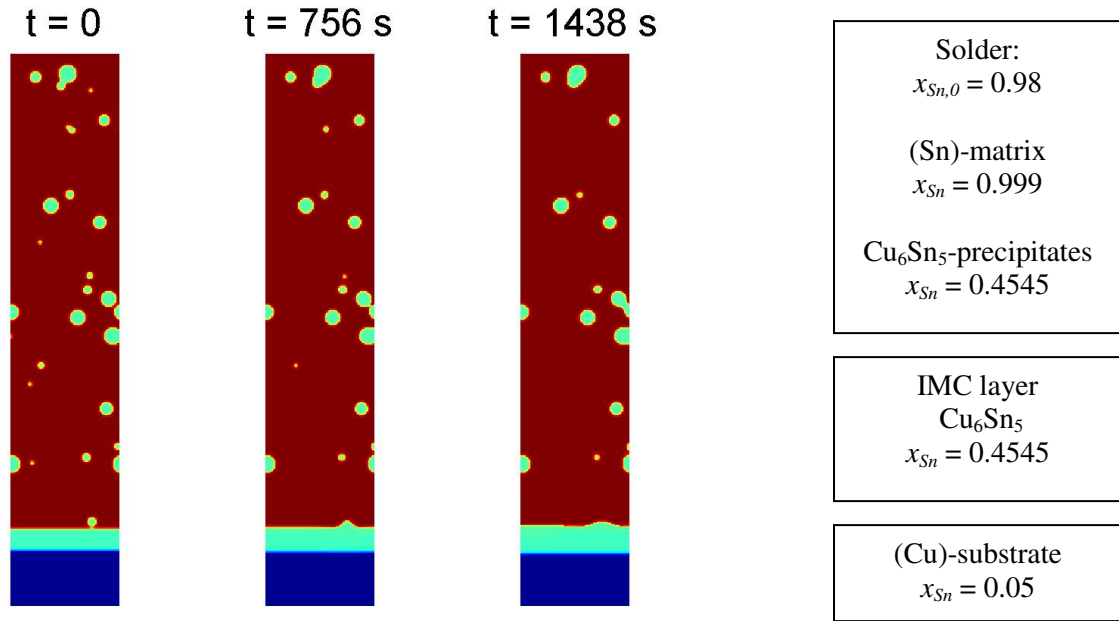


Figure 9: Simulation images of the coarsening of a solder joint formed between a (Cu) substrate and Sn-0.02at%Cu solder.

### Acknowledgments

We gratefully acknowledge FWO – Flanders (NM), OT/07/040 (NM, AS), IWT - Flanders (JH) and the Belgian IUAP-program DISCO (LVH) for financial support. Part of the work was performed in the framework of COST MP0602. Simulations were performed on the High Performance Computer of the K.U.Leuven.

### References

- [1] L.-Q. Chen, Phase-field models for microstructure evolution, *Annu. Rev. Mater. Res.*, Vol 32, 2002, p 113-140.
- [2] K. Thornton, J. Agren and P.W. Voorhees, Modelling the evolution of phase boundaries in solids at the meso- and nano-scales, *Acta Mater.*, Vol 51, 2003, p 5675-5710
- [3] N. Moelans, B. Blanpain and P. Wollants, An introduction to phase field modeling of microstructure evolution, *CALPHAD*, Vol 32, 2008, p 268-294
- [4] N. Moelans, B. Blanpain and P. Wollants, Quantitative phase-field approach for simulating grain growth in anisotropic systems with arbitrary inclination and misorientation dependence, *Phys. Rev. Lett.*, accepted; Quantitative analysis of grain boundary properties in a generalized phase field model for grain growth in anisotropic systems, *Phys. Rev. B*, accepted
- [5] J. Tiaden, B. Nestler, H.J. Diepers and I. Steinbach, The multiphase-field model with an integrated concept for modelling solute diffusion, *Physica D*, Vol 115, 1998, p 73-86

- [6] S.G. Kim, W.T. Kim and T. Suzuki, Phase-field model for binary alloys, *Phys. Rev. E*, Vol 60, 1999, p 7186-7196
- [7] J. Eiken, B. Böttger, I. Steinbach, Multiphase-field approach for multicomponent alloys with extrapolation scheme for numerical application, *Phys. Rev. E*, Vol 73, 2006, p 066122
- [8] S.G. Kim, A phase-field model with antitrapping current for multicomponent alloys with arbitrary thermodynamic properties, *Acta Mater.*, Vol 55, 2007, p 4391-4399
- [9] H.L. Lukas, S.G. Fries and B. Sundman, *Computational thermodynamics: The Calphad Method*, Cambridge 2007, ISBN 0-08-0421296
- [10] T. Veldhuizen, Using C++ template metaprograms, *C++ Report*, Vol. 7, 1995, p 36-43
- [11] D. Abrahams and A. Gurtovoy, *C++ Template Metaprogramming: Concepts, Tools, and Techniques from Boost and Beyond*, Addison-Wesley Professional, 2004
- [12] L.-Q. Chen and J. Shen, Application of semi-implicit Fourier-spectral method to phase field equations, *Comp. Phys. Comm.*, Vol 108, 1998, 147-158
- [13] T. Veldhuizen, Expression Templates, *C++ Report*, Vol. 7, 1995, p 26-31
- [14] L. Vanherpe, N. Moelans, S. Vandewalle and B. Blanpain, Bounding box algorithm for three-dimensional phase-field simulations of microstructural evolution in polycrystalline materials, *Phys. Rev. E*, Vol 76, 2007, p 056702
- [15] N. Moelans, B. Blanpain and P. Wollants, A phase field model for the simulation of grain growth in materials containing finely dispersed incoherent second-phase particles, *Acta Mater.*, Vol 53, 2005, p 1771-1781; Phase field simulations of grain growth in 2-dimensional polycrystalline systems containing finely dispersed incoherent second-phase particles, *Acta Mater.*, Vol 54, 2006, p 1175-1184
- [16] N. Moelans, B. Blanpain and P. Wollants, Pinning effect of second-phase particles on grain growth in polycrystalline films studied by 3-D phase field simulations, *Acta Mater.*, Vol 55, 2007, 2173-2182
- [17] SGTE (Scientific Group Thermodata Europe), <http://www.sgte.org/>

---

\* Corresponding author : nele.moelans@mtm.kuleuven.be